Interplay of morphology, composition, and optical properties of InP-based quantum dots emitting at the 1.55 μm telecom wavelength

C. Carmesin,[1,*] M. Schowalter,[2] M. Lorke,[1] D. Mourad,[1,3] T. Grieb,[2] K. Müller-Caspary,[4] M. Yacob,[5] J. P. Reithmaier,[5] M. Benyoucef,[5] A. Rosenauer,[2,6] and F. Jahnke[1,6]

[1]*Institute for Theoretical Physics, University of Bremen, 28359 Bremen, Germany*

[2]*Institute of Solid State Physics, University of Bremen, 28359 Bremen, Germany*

[3]*Bremen Center for Computational Materials Science, University of Bremen, 28359 Bremen, Germany*

[4]*EMAT, University of Antwerp, Groenenborgerlaan 171, B-2020 Antwerp, Belgium*

[5]*Institute of Nanostructure Technologies and Analytics (INA), CINSaT, University of Kassel, 34132 Kassel, Germany*

[6]*MAPEX Center for Materials and Processes, University of Bremen, 28359 Bremen, Germany*

Results for the development and detailed analysis of self-organized InAs/InAlGaAs/InP quantum dots suitable for single-photon emission at the 1.55 μm telecom wavelength are reported. The structural and compositional properties of the system are obtained from high-resolution scanning transmission electron microscopy of individual quantum dots. The system is composed of almost pure InAs quantum dots embedded in quaternary InAlGaAs barrier material, which is lattice matched to the InP substrate. When using the measured results for a representative quantum-dot geometry as well as experimentally reconstructed alloy concentrations, a combination of strain-field and electronic-state calculations is able to reproduce the quantum-dot emission wavelength in agreement with the experimentally determined photoluminescence spectrum. The inhomogeneous broadening of the latter can be related to calculated variations of the emission wavelength for the experimentally deduced In-concentration fluctuations and size variations.

I. INTRODUCTION

One of the current challenges in the realization of quantum light sources is the systematic extension of the emission energies into the low-loss telecom bands [1]. For the O band at 1.3 μm, this has been accomplished with InAs/InGaAs quantum dots by including a strain-reducing layer [2–4] or by dots-in-a-well structures [5,6]. For the emission at the C band at 1.55 μm, different approaches have been applied successfully to grow InAs quantum dots on InP substrates, such as the double-cap method [7], the insertion of ultrathin GaAs layers [8], or droplet epitaxy [9]. Recently, this goal has been achieved by using InAs/InGaAs/GaAs quantum dots (QDs) [10]. Additionally, a new material system consisting of low-density InAs/InAlGaAs/InP QDs [11,12] has been suggested. Our goal is to characterize this promising material system and to identify dominant contributions to the connection among morphology, composition, electronic, and optical properties. In the following analysis, we employ a combination of theoretical and experimental methods, starting with a structural characterization of individual QDs using quantitative high-resolution scanning transmission electron microscopy (qHRSTEM) [13,14]. The results are used as input for an atomistic tight-binding (TB) model in order to investigate the influences of size and alloy concentration on the emission wavelength. A comparison with the experimentally determined photoluminescence (PL) spectrum shows that the inhomogeneous broadening of the QD ensemble has a strong contribution from In-concentration fluctuations in addition to size variations.

II. EXPERIMENTAL RESULTS

The sample was grown on a (100) InP substrate using a Gen II solid source molecular beam epitaxy system and consists of a 246 nm InP buffer layer deposited at 465 °C followed by a 20-pair distributed Bragg reflector (DBR) grown at 500 °C. Each quarter-wave DBR pair contains a 123 nm thick InP and a 110 nm thick $Al_{0.1}Ga_{0.37}In_{0.53}As$ layer. Subsequently, a 228 nm thick $Al_{0.24}Ga_{0.23}In_{0.53}As$ layer, which is lattice matched to InP, was deposited at 514 °C. For the QDs nominally two monolayers of InAs were deposited at the same temperature. Afterwards, the substrate temperature was reduced to 413 °C using arsenic overpressure which leads to the formation of large and sparse InAs QDs (about 5×10^8 cm^{-2}) as shown in the inset of Fig. 1. The sample was capped by 228 nm InAlGaAs. For additional details see Refs. [11,12]. The formation of InAs QDs also was confirmed by low-temperature (10 K) macro-PL measurements (see Fig. 1) where the emission of the QDs is centered on the telecom C-band wavelength of 1.55 μm.

TEM specimens were prepared using a FEI Nova focused ion beam equipped with a Kleindieck manipulator and investigated using a FEI Titan 80/300 ST equipped with a Fischione high angle annular dark-field (HAADF) detector at 300 kV. For energy-dispersive x rays (EDXs), the specimen was tilted approximately 15° towards the EDAX detector. In and Al concentrations have been measured by qHRSTEM involving normalization to the incident beam intensity and comparison with simulations as described in Refs. [13–15] using the Debye-Waller factor from Ref. [16] and taking into account static atomic displacements [17].

In order to quantify Al and In concentrations from the HRSTEM images, local minima of the experimental image intensity were searched and refined using two perpendicular
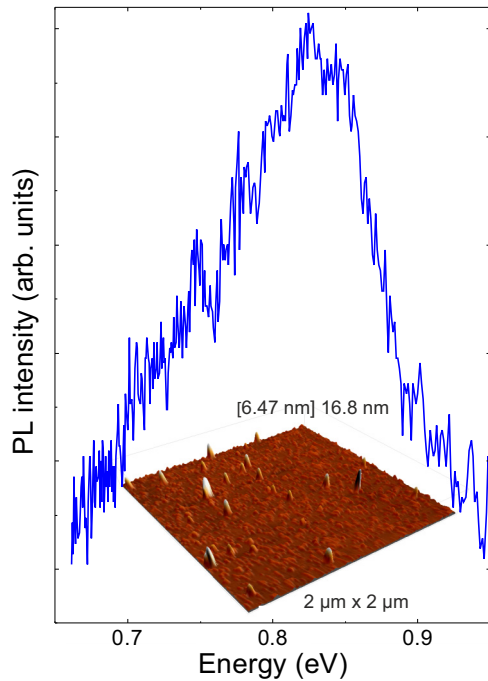
*ccarmesin@itp.uni-bremen.de

FIG. 1. Low-temperature (10 K) macro-PL spectrum taken at an excitation power of 52 W/cm^2. The inset: three-dimensional atomic force microscopy image (2×2 μm^2) of an uncapped QD structure showing a minimum (6.47 nm) and a maximum (16.8 nm) height of the QDs.

one-dimensional parabolian fits. For each position, the experimental normalized lattice plane distance was determined as well as the Voronoi intensity as suggested in Ref. [14]. The In and Al concentrations corresponding to each Voronoi cell can be extracted from the intersection point of the isolines for the measured strain and mean intensity in the reference data set for a known local specimen thickness as described in Refs. [18,19]. This thickness was measured in a reference region in the matrix material below and above the wetting layer and interpolated linearly in the region of the wetting layer. In the case of the quaternary matrix In$_x$Al$_y$Ga$_{1-x-y}$As, the composition has to be measured independently in order to determine the specimen thickness. Using EDX, concentrations of 0.22 Al, 0.25 Ga, and 0.53 In with an error of about ± 0.02 were found confirming the nominal values of 0.24, 0.23, and 0.53 within the error margins of the measurement.

Figure 2(a) shows a HAADF-STEM image of the structure close to the active zone. One can see the last InP layer of the InP/InAlGaAs DBR structure together with the InAlGaAs matrix in which the InAs layer is embedded. The active layer exhibits slight fluctuations of the HAADF intensity indicating the presence of QDs (A and B). An overview image of the active zone between QDs B and C is given in Fig. 2(b). The wetting layer in between the two QDs exhibits fluctuations in both intensity and thickness. Figures 2(c) and 2(d) contain images with larger magnification of QDs A and B. All identified QDs (A–C) exhibit a sharp triangular shape when viewed in [110] zone axis orientation, indicating a pyramidal shape. We measured a side facet angle around 25° towards the basal plane of the QD, indicating the side facets of the pyramid to be ($1\bar{1}3$) planes. The type of surface of the QD is also in
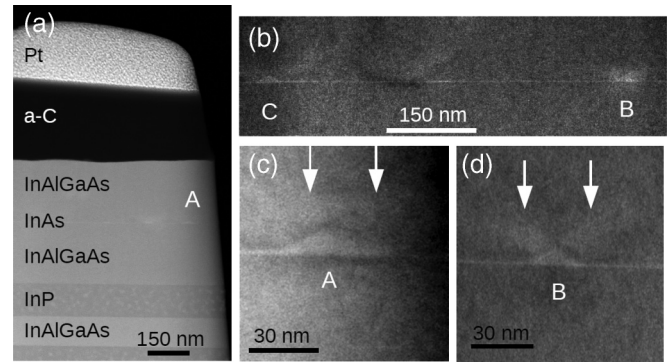

FIG. 2. (a) Overview image of the TEM specimen. (b) Image of the active region including QDs B and C. The wetting layer between the QDs exhibits fluctuations of the In concentration. (c) and (d) Images of QDs A and B, showing a pyramidal contrast of the QDs. For all QDs, we find In diffusion into the top barrier indicated by stripes with slightly increased intensity (marked by the arrows).

accordance with the measured heights and widths of the QDs at their bases. For QD A we determined a width of 55 nm and a height of 12.5 nm. Especially for QD B in Fig. 2(d), regions with an increased intensity (indicated by arrows) evolve into the direction of the side facet normal hinting on a diffusion of In out of the QD towards the InAlGaAs cap layer. The height of the QD found here was slightly smaller than the mean height from antiferromagnetic AFM measurements. However, as the bright stripes above the QDs suggest diffusion from the QDs into the cap layer a shrinkage of QDs during cap layer overgrowth can be expected. The two other identified QDs appeared to be smaller so that we focused on the largest QD for which the height was closest to the mean height from the AFM results.

In order to characterize the composition within the wetting layer and QD, the method described above was applied to HRSTEM images. Figures 3(a) and 3(b) represent the In and Al concentration maps obtained in the vicinity of QD A. As an overall trend, the In concentration within the QD and wetting-layer region increases whereas the Al concentration is significantly reduced. For the wetting layer, In and Al concentrations of 0.70 ± 0.05 and 0.15 ± 0.05 are determined.

Horizontal line scans from the data in Figs. 3(a) and 3(b) through the largest extension of the QD are provided in Figs. 3(c) and 3(d). Approximately constant In concentration within the QD area and increasing Al concentration from the wetting layer towards the top of the QD are obtained.

The results in Fig. 3 are averages in the transmission direction through the TEM lamella, which contains the wetting layer perpendicular to the specimen surface as well as the side view of the QD surrounded by matrix material. Hence, in the transmission averages, the full wetting-layer contribution is obtained, whereas the QD contribution decreases from the base to the top at the expense of matrix material contributions. In order to obtain the true In and Al concentrations within the QD, projections through a three-dimensional model QD need to be compared with the observed transmission scans. The results of the correspondingly deduced QD model are summarized in Fig. 4.
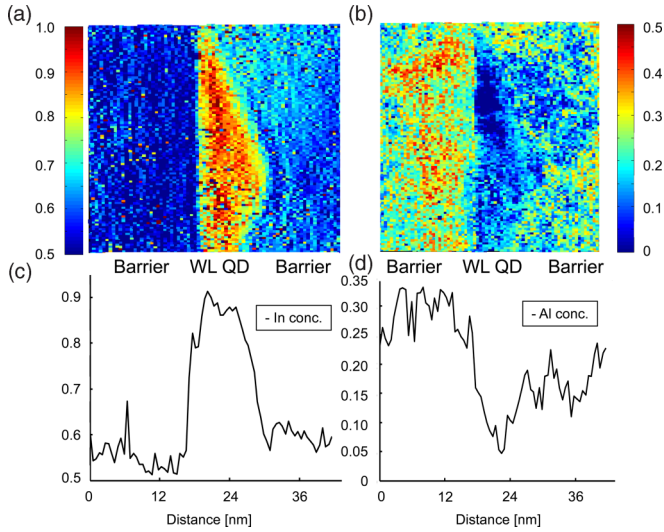
FIG. 3. (a) In and (b) Al concentration maps from a scan across the TEM lamella in the vicinity of QD A. The given In and Al concentrations represent averages in transmission direction through the TEM specimen. Results of horizontal line scans through the center of the QD in panels (a) and (b) are shown as (c) and (d).

As a side note to Fig. 3(a), above the side facets a slightly increased In concentration is observed, which corroborates the discussed In diffusion out of the QD. The high noise level in the Al map can be attributed to the weak dependence of the HAADF intensity on the Al concentration.

III. THEORETICAL ANALYSIS

For electronic state calculations of semiconductor QDs, both continuum models [20–22] and atomistic TB [23–26] have been used successfully. In recent examples, the influence of the local symmetry on light-hole–heavy-hole coupling in
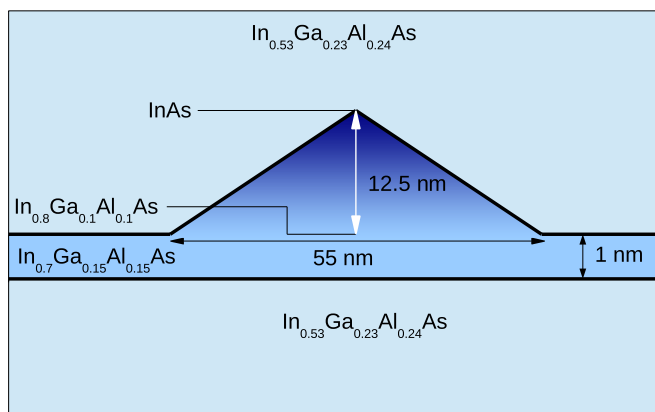

FIG. 4. Geometry as obtained from HRSTEM analysis. The pyramidal QD is situated on top of the wetting layer and shows a linearly increasing In concentration from bottom (lighter blue) to top (darker blue), whereas the Ga and Al contents decrease accordingly. The wetting layer has a height of 1 nm and a slightly smaller In content than the bottom of the QD. The QD-wetting-layer system is embedded in a quaternary barrier material with an even smaller In concentration (light blue).

nanostructures has been demonstrated [27], and piezoelectric properties of zinc-blende QDs [28] have been investigated. Continuum $\vec{k} \cdot \vec{p}$ models have been used to study the influence of the fields generated by charged defects in the vicinity of QDs [29] as well as the properties of (111)-oriented QDs [30,31]. Since our experimental investigations involve a HRSTEM characterization of geometry and alloy concentration of individual QDs with atomic resolution, we use an atomistic TB approach.

We model the QD by placing individual In, Ga, Al, and As atoms on a zinc-blende lattice in a way that the experimentally determined geometry and concentration maps are reproduced. The used geometry and spatial distribution of alloy concentrations are summarized in Fig. 4. For practical calculations, the QD is embedded in a sufficiently large supercell (see the Supplemental Material [32], which includes Refs. [33–39]) with periodic boundary conditions. At each cation lattice site, the atom types (In, Ga, and Al) are placed randomly according to the local target concentrations. Following this procedure, different random realizations with the same local alloy concentration profile are generated. For each individual realization, we perform the complete calculation consisting of the strain-field simulation and TB diagonalization, leading to a set of single-particle energies. Due to the large In concentration inside the QD and the large number of atoms, energy fluctuations are rather small and remain within the size of the used data points in Fig. 6 discussed below. To determine the local displacements of the individual atoms due to strain effects, we employ a valence force field calculation using the LAMMPS code [40]. To achieve convergence for the relaxed geometry, we utilize a supercell of dimensions $140 \times 140 \times 120 \text{ nm}^3$, containing about 10^8 atoms. The calculation is performed until a force tolerance of 10^{-3} eV/Å or a relative energy tolerance of 10^{-16} is reached. A commonly used harmonic pair interaction for ternary material systems is given by the Keating potential [41]. For our quaternary material system, we use the Tersoff potential [42] with a parametrization from Ref. [43] as this bond-order potential includes correction terms beyond a harmonic approximation and aspects of the bond chemistry.

The resulting strain field is displayed in Fig. 5. For ε_{xx} (left column), there is compressive strain inside the QD and tensile strain propagating into the barrier, whereas for ε_{zz} (right column), the opposite situation is observed. The fluctuations in Figs. 5(a) and 5(b) stem from the different lattice constants of the individual atoms in the quaternary barrier. This causes a finite strain with respect to the average lattice constant a_{InP} for any distance between two neighboring atoms in the barrier. The absolute magnitude of strain in the quaternary barrier is about half as large as in the binary material system. This is caused by the differences of the lattice constants in the quaternary barrier compared to the binary situation: $|a_{\text{InAs}} - a_{\text{InP}}| \approx 1/2|a_{\text{InAs}} - a_{\text{GaAs}}|$.

The resulting atomic positions, including strain can be incorporated into the TB Hamiltonian. For this purpose, the rule of Harrison [45] commonly is applied in which originally an exponential scaling of $(\frac{r_0}{r})^\eta$ with $\eta = 2$ was proposed. Here, r_0 and r are the unstrained and strained atomic distances. Depending on the material and the used basis set for its description, a different choice for the exponent might be necessary. We employ the sp^3s^* model of Ref. [46]
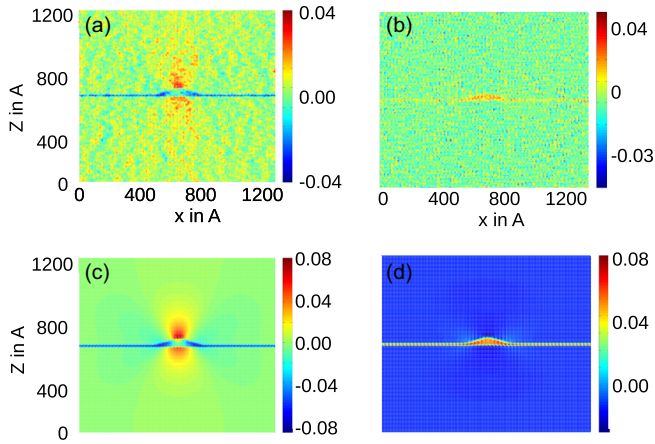
FIG. 5. (a) and (b) Calculated strain components ε_{xx} and ε_{zz} along a cross section through the center of the investigated quaternary QD of Fig. 4. (c) and (d) Strain components ε_{xx} and ε_{zz} for a binary InAs/GaAs QD of the same size and shape shown for comparison. To determine the strain, we follow Ref. [44] and use $\varepsilon_{ij} = \frac{a_{\mathrm{InP}}}{a_{\mathrm{ref}}} \frac{a_{ij}^{\mathrm{final}} - a_{\mathrm{InP}}}{a_{\mathrm{InP}}} - \delta_{ij} \frac{a_{\mathrm{ref}} - a_{\mathrm{InP}}}{a_{\mathrm{ref}}}$ where an average lattice constant of $a_{\mathrm{ref}} = a_{\mathrm{InP}}$ in the quaternary barrier and $a_{\mathrm{ref}} = a_{\mathrm{InAs}}$ inside the QD is assumed. The lattice constant a_{ij}^{final} after the relaxation is obtained by taking the component i of the difference vector between neighboring atoms along direction j.

using nearest neighbors and spin-orbit coupling [47]. For this basis set, values of $\eta_{\mathrm{InGaAs}} = 2.9$ and $\eta_{\mathrm{AlGaAs}} = 3.4$ are chosen following Refs. [48,49], respectively. These values were obtained from experiments in which pressure on the bulk material was exerted and the results were reproduced with the sp^3s^* TB basis set.

For electronic state calculations, we utilize the sp^3s^* TB model with a parametrization from Refs. [33,34]. Valence-band offsets $\Delta_{\mathrm{v}}^{\mathrm{InAs}} = 0.06$ and $\Delta_{\mathrm{v}}^{\mathrm{AlAs}} = -0.59$ eV with respect to GaAs are obtained from the methods in Refs. [50,51]. The TB model consists of on-site terms (orbital energies) and coupling terms (overlap), which are chosen to best reproduce the binary bulk band structure. The TB parametrization of bulk crystals for the sp^3s^* nearest-neighbor basis set is only available for binary compounds, such as GaAs, InAs, and AlAs. This already poses the question, how bulk crystals of quaternary InGaAlAs should be treated in such a model. The cation on-site matrix elements and the coupling matrix elements can be chosen according to the elements on the respective lattice sites. However, the anion on-site matrix elements of As vary for the different binary compounds, which necessitates an averaging procedure. One option is to average according to the nearest neighbors on the tetrahedron. Although this procedure gives satisfactory results for the bowing curves [52–54] of a bulk material calculation, it leads to band gaps that strongly depart from the experimentally observed ones for nanostructures. We interpret this as a shortcoming of the nearest-neighbor approximation within this scheme for nanostructures. Alternatively, in addition to the anion on-site matrix elements, one also can average the coupling matrix elements within a tetrahedron. This approach does not only reproduce in a satisfactory way the bulk material bowing curves, but also enhances the agreement with
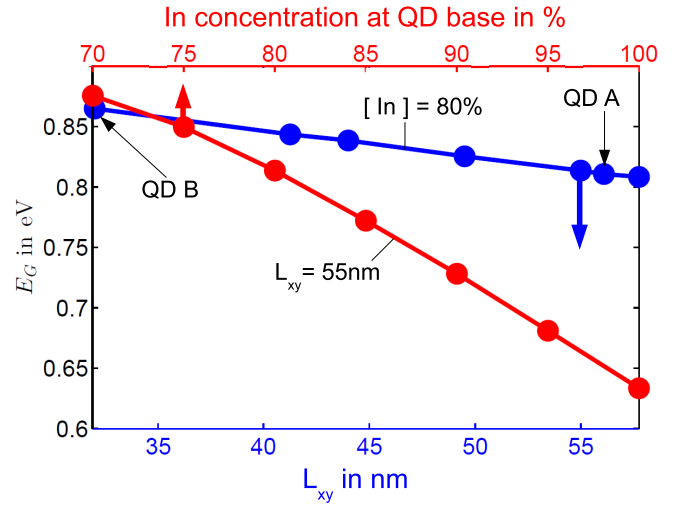

FIG. 6. Variation of single-particle/quasiparticle band-gap E_G for different QD side lengths of the rectangular basis with a constant diameter-to-height ratio (bottom axis) and for different In concentrations (top axis) at the base of the pyramid.

experiment for nanostructures considerably. Therefore, it was employed in our investigations.

Diagonalization of the resulting TB Hamiltonian provides the eigenenergies of the confined electron and hole QD states. The difference between the lowest electron and the highest hole state defines the single-particle/quasiparticle band gap. This energy is lowered by the exciton binding energy originating from electron-hole Coulomb interaction. For the representative QD structure (see Fig. 4) we have performed a configuration interaction calculation [26] with 50 states for both electrons and holes and obtained exciton binding energies of about 30 meV. This number is small compared to the overall energy scale (see Fig. 1) and almost constant for different QDs. Consequently, the subsequent discussion will be conducted with respect to the single-particle/quasiparticle band-gap E_G.

For the structure in Fig. 4, we obtain $E_G = 810$ meV (see Fig. 6). This energy is near the maximum of the PL spectrum (see Fig. 1), which supports that the corresponding morphology and composition are typical for the QD ensemble. This geometry is used as a starting point for the subsequent investigations of the influences of size and concentration fluctuations on the single-particle/quasiparticle band gaps of the QDs within the ensemble.

For the analysis of size fluctuations, we consider a constant diameter-to-height ratio for all QDs. According to Fig. 6, fluctuations of the QD size within a range of 25% result in a shift of 30 meV. Size fluctuations corresponding to the difference between QDs A and B result in energy fluctuations of about 60 meV. Even the assumption of yet larger size fluctuations alone cannot explain the observed inhomogeneous broadening in Fig. 1.

For the analysis of concentration fluctuations, the QD structure of Fig. 4 with a fixed size is used. In different calculations for individual QDs, we vary the In concentration at the base of the pyramidal QD. In all cases, the In concentration increases linearly to 100% at the top, whereas the remaining cation lattice sites are uniformly distributed among Ga and

Al. Figure 6 shows that possible fluctuations cover an energy range of over 200 meV. These fluctuations can explain the main contribution to the inhomogeneous broadening of the spectrum in Fig. 1. In the limit of a pure InAs quantum dot, we obtain a single-particle/quasiparticle band gap of about $E_G = 630$ meV (see Fig. 6). This value corresponds to the low-energy edge of the experimental PL spectrum.

The strong influence of concentration fluctuations is a manifestation of the fact that the relative conduction band-edge positions $E_c = E_g + E_v$ of AlAs ($E_c \sim 2.4$ eV), GaAs ($E_c \sim 1.5$ eV), and InAs ($E_c \sim 0.4$ eV) differ substantially for the given valence-band alignment in the quaternary material.

IV. CONCLUSION

In conclusion, we have identified the QD geometry and size as well as alloy concentrations for a representative structure of a novel quaternary InAlGaAs material system using qHRSTEM. Atomistic TB simulations based on a TEM-determined morphology show that composition fluctuations within the QD ensemble can modify the emission energy by about 200 meV. In these rather large QDs, size fluctuations have a somewhat reduced influence. The identified size difference between QDs A and B results in an emission energy difference of about 60 meV. The combination of both effects can explain the experimentally observed inhomogeneous broadening in the emission spectrum.

[1] S. Gordon, M. Yacob, J. P. Reithmaier, M. Benyoucef, and A. Zrenner, Appl. Phys. B **122**, 37 (2016).

[2] K. Nishi, H. Saito, S. Sugou, and J.-S. Lee, Appl. Phys. Lett. **74**, 1111 (1999).

[3] M. B. Ward, T. Farrow, P. See, Z. L. Yuan, O. Z. Karimov, A. J. Bennett, A. J. Shields, P. Atkinson, K. Cooper, and D. A. Ritchie, Appl. Phys. Lett. **90**, 063512 (2007).

[4] E. Goldmann, M. Paul, F. F. Krause, K. Müller, J. Kettler, T. Mehrtens, A. Rosenauer, M. Jetter, P. Michler, and F. Jahnke, Appl. Phys. Lett. **105**, 152102 (2014).

[5] V. M. Ustinov, N. A. Maleev, A. E. Zhukov, A. R. Kovsh, A. Y. Egorov, A. V. Lunev, B. V. Volovik, I. L. Krestnikov, Y. G. Musikhin, N. A. Bert *et al.*, Appl. Phys. Lett. **74**, 2815 (1999).

[6] H. Y. Liu, M. Hopkinson, C. N. Harrison, M. J. Steer, R. Frith, I. R. Sellers, D. J. Mowbray, and M. S. Skolnick, J. Appl. Phys. **93**, 2931 (2003).

[7] T. Miyazawa, K. Takemoto, Y. Sakuma, S. Hirose, T. Usuki, N. Yokoyama, M. Takatsu, and Y. Arakawa, Jpn. J. Appl. Phys. **44**, L620 (2005).

[8] S. Anantathanasarn, R. Nötzel, P. J. van Veldhoven, T. J. Eijkemans, and J. H. Wolter, J. Appl. Phys. **98**, 013503 (2005).

[9] J. Skiba-Szymanska, R. M. Stevenson, C. Varnava, M. Felle, J. Huwer, T. Müller, A. J. Bennett, J. P. Lee, I. Farrer, A. B. Krysa *et al.*, Phys. Rev. Appl. **8**, 014013 (2017).

[10] M. Paul, F. Olbrich, J. Höschele, S. Schreier, J. Kettler, S. L. Portalupi, M. Jetter, and P. Michler, Appl. Phys. Lett. **111**, 033102 (2017).

[11] M. Benyoucef, M. Yacob, J. P. Reithmaier, J. Kettler, and P. Michler, Appl. Phys. Lett. **103**, 162101 (2013).

[12] M. Yacob, J. P. Reithmaier, and M. Benyoucef, Appl. Phys. Lett. **104**, 022113 (2014).

[13] A. Rosenauer, K. Gries, K. Müller, A. Pretorius, M. Schowalter, A. Avramescu, K. Engl, and S. Lutgen, Ultramicroscopy **109**, 1171 (2009).

[14] A. Rosenauer, T. Mehrtens, K. Müller, K. Gries, M. Schowalter, P. V. Satyam, S. Bley, C. Tessarek, D. Hommel, K. Sebald *et al.*, Ultramicroscopy **111**, 1316 (2011).

[15] F. F. Krause, M. Schowalter, T. Grieb, K. Müller-Caspary, T. Mehrtens, and A. Rosenauer, Ultramicroscopy **161**, 146 (2016).

[16] M. Schowalter, A. Rosenauer, J. T. Titantah, and D. Lamoen, Acta Cryst. A **65**, 5 (2009).

[17] M. Schowalter, K. Müller, and A. Rosenauer, Acta Cryst. A **68**, 68 (2012).

[18] K. Müller, M. Schowalter, A. Rosenauer, D. Hu, D. M. Schaadt, M. Hetterich, P. Gilet, O. Rubel, R. Fritz, and K. Volz, Phys. Rev. B **84**, 045316 (2011).

[19] T. Grieb, K. Müller, R. Fritz, M. Schowalter, N. Neugebohrn, N. Knaub, K. Volz, and A. Rosenauer, Ultramicroscopy **117**, 15 (2012).

[20] H. Fu, L.-W. Wang, and A. Zunger, Phys. Rev. B **57**, 9971 (1998).

[21] O. Stier, M. Grundmann, and D. Bimberg, Phys. Rev. B **59**, 5688 (1999).

[22] A. Schliwa, M. Winkelnkemper, and D. Bimberg, Phys. Rev. B **76**, 205324 (2007).

[23] J.-M. Jancu, R. Scholz, F. Beltram, and F. Bassani, Phys. Rev. B **57**, 6493 (1998).

[24] R. Viswanatha, S. Sapra, T. Saha-Dasgupta, and D. D. Sarma, Phys. Rev. B **72**, 045333 (2005).

[25] S. Schulz and G. Czycholl, Phys. Rev. B **72**, 165317 (2005).

[26] M. Zieliński, M. Korkusiński, and P. Hawrylak, Phys. Rev. B **81**, 085301 (2010).

[27] J.-W. Luo, G. Bester, and A. Zunger, Phys. Rev. B **92**, 165301 (2015).

[28] S. Schulz, M. A. Caro, E. P. O'Reilly, and O. Marquardt, Phys. Status Solidi B **249**, 521 (2012).

[29] G. Hönig, S. Rodt, G. Callsen, I. A. Ostapenko, T. Kure, A. Schliwa, C. Kindel, D. Bimberg, A. Hoffmann, S. Kako *et al.*, Phys. Rev. B **88**, 045309 (2013).

[30] A. Schliwa, M. Winkelnkemper, A. Lochmann, E. Stock, and D. Bimberg, Phys. Rev. B **80**, 161307 (2009).

[31] O. Marquardt, E. P. O'Reilly, and S. Schulz, J. Phys.: Condens. Matter **26**, 035303 (2014).

[32] See Supplemental Material at http://link.aps.org/supplemental/10.1103/PhysRevB.96.235309 for a detailed discussion of the supercell size and the TB parameters.

[33] Y. Wei and M. Razeghi, Phys. Rev. B **69**, 085316 (2004).

[34] T. B. Boykin, G. Klimeck, R. C. Bowen, and R. Lake, Phys. Rev. B **56**, 4102 (1997).

[35] I. Broser, R. Broser, H. Finkenrath, R. R. Galazka, H. E. Gumlich, A. Hoffmann, J. Kossut, E. Mollwo, H. Nelkowski, G. Nimtz *et al.*, *Physics of II–VI and I–VII Compounds, Semimagnetic Semiconductors*, Landolt-Bornstein: New Series (Springer, Berlin, 1982).

[36] G. Kresse and J. Hafner, Phys. Rev. B **47**, 558 (1993).

[37] G. Kresse and J. Furthmüller, Comput. Mater. Sci. **6**, 15 (1996).

[38] G. Kresse and D. Joubert, Phys. Rev. B **59**, 1758 (1999).

[39] Y.-S. Kim, M. Marsman, G. Kresse, F. Tran, and P. Blaha, Phys. Rev. B **82**, 205212 (2010).

[40] S. Plimpton, J. Comput. Phys. **117**, 1 (1995).

[41] P. N. Keating, Phys. Rev. **149**, 674 (1966).

[42] J. Tersoff, Phys. Rev. B **39**, 5566 (1989).

[43] D. Powell, M. A. Migliorato, and A. G. Cullis, Phys. Rev. B **75**, 115202 (2007).

[44] S. Hackenbuchner, *Elektronische Struktur von Halbleiter-Nano-bauelementen im Thermodynamischen Nichtgleichgewicht*, Selected topics of Semiconductor Physics and Technology (Walter Schottky Institut der Technischen Universität München, München, 2002).

[45] S. Froyen and W. A. Harrison, Phys. Rev. B **20**, 2420 (1979).

[46] P. Vogl, H. P. Hjalmarson, and J. D. Dow, J. Phys. Chem. Solids **44**, 365 (1983).

[47] D. Chadi, Phys. Rev. B **16**, 790 (1977).

[48] W. Jaskólski, M. Zieliński, G. W. Bryant, and J. Aizpurua, Phys. Rev. B **74**, 195339 (2006).

[49] R. B. Capaz, J. P. von der Weid, and B. Koiller, Appl. Phys. Lett. **60**, 704 (1992).

[50] D. Mourad, J.-P. Richters, L. Gérard, R. André, J. Bleuse, and H. Mariette, Phys. Rev. B **86**, 195308 (2012).

[51] D. Mourad, J. Appl. Phys. **113**, 123705 (2013).

[52] I. Vurgaftman, J. R. Meyer, and L. R. Ram-Mohan, J. Appl. Phys. **89**, 5815 (2001).

[53] G. P. Donati, R. Kaspi, and K. J. Malloy, J. Appl. Phys. **94**, 5814 (2003).

[54] M. Guden and J. Piprek, Modell. Simul. Mater. Sci. Eng. **4**, 349 (1996).